ADVANCED MATERIALS TECHNOLOGIES
www.advmattechnol.de

Continuous Embedded Droplet Printing in Yield-Stress Fluids for Pharmaceutical Drug Particle Synthesis

Arif Z. Nelson, Jiaxun Xie, Saif A. Khan, and Patrick S. Doyle**

Embedded droplet printing is a recent mode of generating and processing droplets within yield-stress fluids. This technique has shown promise for performing sensitive processes like pharmaceutical crystallization, as well as chemical synthesis and biological experimentation due to the unique ability to process droplets that are quiescently suspended. Despite improving on conventional microfluidic technologies in numerous ways, current embedded droplet printing methods are limited to batch processes, severely hampering their overall utility. A new platform that enables continuous production of embedded droplets is presented and characterized. This platform expands the capabilities of embedded droplet printing and allows for its application to areas of continuous materials discovery, screening, and manufacturing. Here, the platform is used for the rapid production of pharmaceutical particles that are highly spherical and uniform, key targets for flowability, and ultimately manufacturability of pharmaceutical drug products. The presented platform achieves a maximum throughput of over 100 g per day, enabling characterization of the superior powder flow properties. The available operating space of this platform is demonstrated for an antisolvent crystallization process with an anti-malarial drug. This understanding provides design guidelines for how similar platforms may be engineered for precise, rapid, customized, and distributed manufacturing of drug particles with superior flowability.

1. Introduction

Embedded droplet printing is a recently developed technique for the generation and processing of droplets that are suspended within a fluid bath.[1] This technique functions by utilizing a class of rheologically complex materials known as "yield-stress fluids;" these materials exhibit a dramatic form of shear-thinning, reversibly transitioning from solid-like to fluid-like at a critical applied stress.[2] Yield-stress fluids are an extremely useful material class, enabling numerous applications including surface coatings, various food and consumer products, injectable drug delivery,[3–5] and various forms of 3D printing.[6–9] By translating a nozzle submerged in a bath of yield-stress fluid while simultaneously injecting an immiscible phase, embedded droplets can be generated. The movement of the nozzle yields and fluidizes the bath, allowing droplets to form due to the surface tension of the injected phase with the bath material. After forming, droplets are statically suspended in place due to the effective yield stress of the bath exceeding the buoyant stress on the droplets,[10–12] and are spatially isolated and stable even without the use of surfactants. Previous work has established the available operating space and the relationship between nozzle movement speed and droplet diameter for a model pairing of a yield-stress fluid and immiscible injected phase.[1]

Embedded droplet printing is an effective method to resolve many persistent challenges of conventional fluidic manipulation techniques. Advantages include a freedom from fixed geometric boundaries and complex device manufacturing, droplet stabilization without molecular surfactants, and the ability to selectively manipulate and process individual droplets. Because of these beneficial qualities, embedded droplet printing has demonstrated unique functionality in a wide variety of fluidic manipulation applications including chemical synthesis

Dr. A. Z. Nelson, Prof. P. S. Doyle
Critical Analytics for Manufacturing Personalized-Medicine
Singapore-MIT Alliance for Research and Technology
Singapore 138602, Singapore
E-mail: pdoyle@mit.edu

The ORCID identification number(s) for the author(s) of this article can be found under https://doi.org/10.1002/admt.202001245.

DOI: 10.1002/admt.202001245

Dr. A. Z. Nelson, Prof. S. A. Khan, Prof. P. S. Doyle
Campus for Research Excellence and Technological Enterprise
Singapore 138602, Singapore
E-mail: saifkhan@nus.edu.sg

J. Xie, Prof. S. A. Khan
Department of Chemical and Biomolecular Engineering
National University of Singapore
Singapore 117585, Singapore

Prof. P. S. Doyle
Department of Chemical Engineering
Massachusetts Institute of Technology
Cambridge, MA 02139, USA

and screening, biological assays, and particle synthesis. There are many techniques for droplet generation and processing including open and off-chip microfluidic systems,[13,14] in-air microfluidics,[15] and droplet formation and deposition at a fluid interface.[16–19] However, embedded droplet printing is the only method (other than a microgravity environment) that allows for droplet processing in an "absolutely quiescent" state, namely the elimination of exterior convective forces as well as essentially indefinite spatial isolation of droplets from each other and from any boundaries of the bath material.

For manufacturing pharmaceutical drug products such as tablets and injectables, a highly prized intermediate outcome is to have particles of crystallized active pharmaceutical ingredient (API) that are as uniformly sized and as spherical as possible. Broad particle size distributions lead to wide variability in terms of drug release and absorption,[20] and sphericity has been demonstrated to correlate with improved tabletability as well as flowability.[21,22] Flowability in particular is an incessant and major concern in pharmaceutical manufacturing since it is difficult to meter out a precise amount of a poorly flowing drug powder.[23] Batch methods can struggle to produce uniform spherical particles, and instead often result in granules of agglomerated crystals that may have irregular shapes or wide size distributions.[24] Microfluidic emulsion approaches to spherical crystallization have provided significant improvements in terms of morphology,[25–27] and also synergize with a broader movement of pharmaceutical manufacturing towards continuous processes due to their advantages in terms of flexibility in production scale, more consistent product quality, and increased efficiency.[23,28,29] However, even in microfluidic platforms, crystalline particles often still have noticeable deviations from sphericity due to the deforming effects of viscous drag,[1] and unintended nucleation and aggregation can occur when droplets come into contact with each other or solid surfaces. Additionally, surfactants are typically required in microfluidic systems to ensure droplet stability, but have been shown to significantly affect crystallization behavior[30] and are often an unwanted ingredient in a final drug powder.

Embedded droplet printing maintains many of the advantages of conventional microfluidic techniques including the ability to precisely control small volumes of high-value pharmaceutical solution, but allows for crystallization to occur under absolutely quiescent conditions and without surfactants. After crystallization has completed, triggered collapse of the yield-stress fluid bath enables convenient recovery of the particles. This unique combination of conditions and capabilities approaches an ideal environment for performing sensitive processes like pharmaceutical crystallization, and in our prior work, we established a method for producing API particles that are as uniform and spherical as possible via antisolvent crystallization of embedded droplets.[1] Critically, however, this method was a non-continuous, batch process. Though the obtained particles were morphologically superior to those obtained via conventional methods, the capability for continuous processing—a major and often intrinsic advantage of microfluidic techniques—was lost. Indeed, the batch nature of the experimental platform made it untenable to produce amounts of material substantial enough to establish a quantitative impact on powder flowability, behavior that is fundamentally important for drug product manufacturability. Developing a way of continuously producing embedded droplets would significantly increase the utility of the developed methods for meaningful applications that include not just manufacturing, but also materials discovery and screening.

In this work, we present a new platform that enables the continuous production of embedded droplets, greatly expanding the functionality of embedded droplet printing. We apply this new platform of continuous embedded droplet printing towards the synthesis of crystallized pharmaceutical particles. We present and validate the constraints on the various operating regimes that arise for this unique platform in order to maximize our mass throughput of pharmaceutical particles for a subset of printing parameters. With this platform, we gain the capability to easily produce gram-scale amounts of free-flowing drug powder that we then characterize using powder rheology measurements. By establishing and understanding the operating space for this type of platform, we map out how similar systems may be designed and engineered to enable precise, rapid, customized, and distributed manufacturing of drug particles with superior flowability and processability.

2. Results and Discussion

Shown schematically in **Figure 1**a, we achieve continuous production via an open-channel flow setup; a walled conveyor belt that carries a film of yield-stress fluid into which an immiscible or partially miscible solution is injected. To produce pharmaceutical particles, we adapt the established antisolvent crystallization method to this platform, printing a solution of hydrophobic API dissolved in a solvent that is partially miscible with the aqueous yield-stress fluid (the antisolvent). The partially miscible solvent is extracted into the bath via diffusion, leaving behind a supersaturated hydrophobic drug solution that solidifies into particles that are collected downstream. Figure 1b depicts the physical platform and the key components; as shown in the inset figure and Videos S1 and S2, Supporting Information, the robotic arm moves horizontally across the open channel, generating rows of embedded droplets. Note that if the fluid film did not possess a yield stress, the printed droplets would immediately rise to the free surface due to their lower density and burst.[25,31] The robotic arm, conveyor belt, and syringe pump are synchronized and controlled through a custom LabVIEW program (see Supporting Information for details). We control the deposition rate of the yield-stress fluid to extrude it as a film of constant thickness at the same movement speed as the conveyor belt, constrained by the sidewalls.

2.1. Printing Pattern Design

As shown in **Figure 2**a, we program the nozzle to repeat an X-shaped pattern designed such that the nozzle translates along the longitudinal axis at the same speed as the fluid film. This results in parallel lines of droplets with regular spacing

$$\delta = \frac{W_B}{V_P} V_B \left(1 + \frac{V_B}{V_P}\right) \tag{1}$$

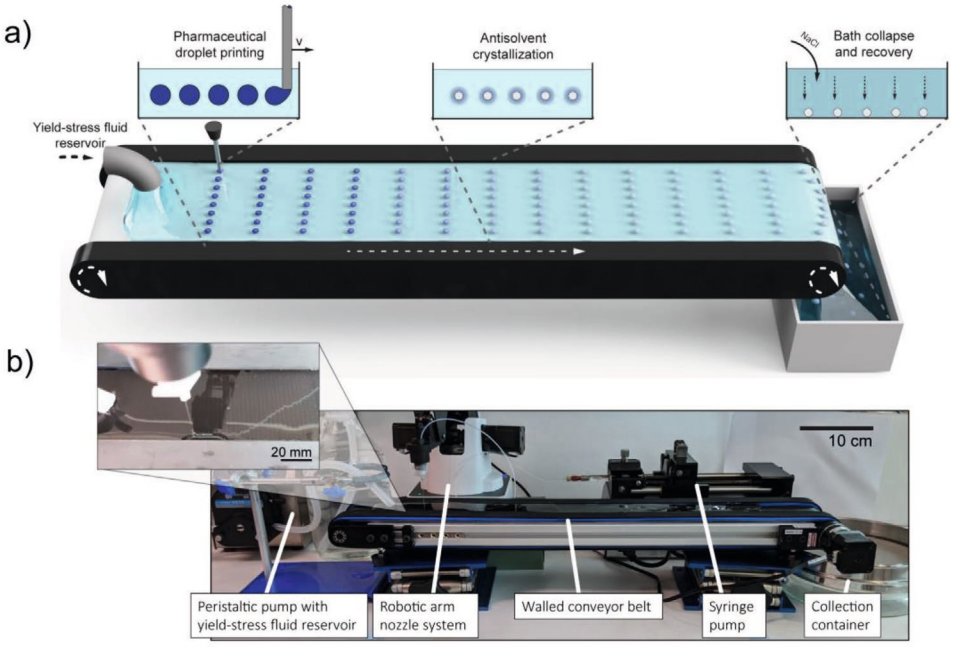

Figure 1. a) Schematic concept of continuous embedded droplet printing for pharmaceutical particle manufacturing. A film of yield-stress fluid suspends printed droplets of an appropriate pharmaceutical drug solution, enabling absolutely quiescent crystallization of spherical particles. After undergoing antisolvent crystallization, the collected solid particles are recovered by triggering the collapse of the bath material. b) Benchtop platform with labeled key components. Inset graphic (also Video S1, Supporting Information) depicts the droplet generation area. We envision similar platforms to enable rapid, customized, and distributed drug manufacturing.

where the width of the printing pattern in the transverse direction is W_B, the nozzle movement speed is V_P, and the belt/film movement speed is V_B. For slow belt speeds relative to the nozzle speed, this equation reduces to

$$\delta = \frac{W_B}{V_P} V_B \tag{2}$$

The regular spacing of a representative printing process is shown in Figure 2b and it ensures that each row experiences consistent diffusion conditions. A more naïve printing approach might be to only move the nozzle in the transverse direction; however, this would result in a triangular wave pattern (Figure S1, Supporting Information). In this case, droplets at the edges of the belt would be much more closely spaced and inhibit each other's ability to diffuse out solvent; for large droplet sizes, this could also lead to coalescence as droplets are essentially printed on top of each other. With our chosen printing pattern, not only do we achieve a more consistent product, but we are able to easily and more

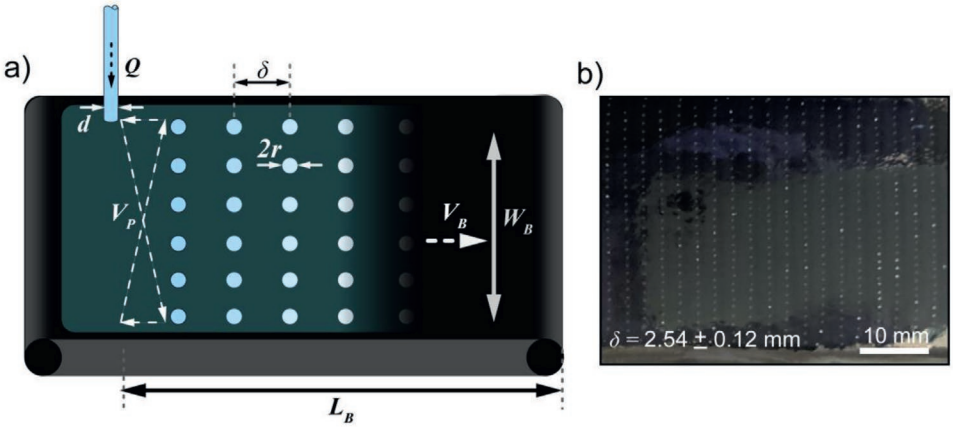

Figure 2. a) Schematic of the various printing and geometric parameters that determine the operating regimes for this platform. Not depicted is the yield-stress fluid film thickness, H. The programmed X-shaped printing pattern results in parallel lines of droplets and regular row spacing, δ, for consistent crystallization conditions. b) Image showing a representative printing setup where $V_P = 1000$ mm min^{-1}, $V_B = 1$ mm s^{-1}, and $W_B = 40$ mm. Using Equation (1), the calculated row spacing, δ, is 2.54 mm, which is consistent with the measured average spacing.

systematically explore the operating regimes of this platform for droplets with a given limit of solubility in the yield-stress fluid film.

2.2. Processing Map of Continuous Embedded Droplet Crystallization

In this section, we consider the theoretical boundaries of our platform when applied to antisolvent crystallization and validate them by systematically exploring process outcomes for different sized droplets and belt speeds. For controlling the size of droplets, in our previous work, we established that droplet size decreases with increasing print speed, and increases with nozzle diameter, d, and injection flowrate, Q.[1] In the range of belt speeds that we test, we do not observe an effect on the nominal droplet size.

2.2.1. Theoretical Boundaries

Due to the absolutely quiescent nature of this platform, supersaturation and ultimately crystallization of the droplets occurs purely due to diffusion, allowing us to model the theoretical boundaries of the processing map for this system appropriately. When performing antisolvent crystallization, we must allow a sufficient time for the solvent contained in the droplets to diffuse into the antisolvent yield-stress fluid. Thus, we expect that the amount of time that a droplet of radius, r, must be on the belt should exceed the characteristic diffusion time and we obtain

$$\frac{L_B}{V_B} > a\frac{(2r)^2}{D} \tag{3}$$

where L_B is the effective length of the conveyor belt, and D is the diffusivity of the solvent in the antisolvent. The fit parameter a is material system specific and depends on the initial loading and solubility of the API in the solvent. The second limit to consider is the proximity of rows of droplets. As mentioned previously for a naïve printing pattern, droplets in too close proximity will inhibit diffusion, reaching a local solubility limit of the solvent in the bath material. Here, we expect that the row spacing, δ, must be some factor, b, greater than the droplet size, i.e.

$$\delta > br \tag{4}$$

here b is again a material system specific parameter that depends on the solubility limit of the solvent in the antisolvent, the yield-stress fluid film thickness, H, as well as the factors that influence the parameter a. Combined, these coupled limits demonstrate the need to thoroughly map the operating space for this platform and application. As an example, if a droplet is sized such that it does not have sufficient time to crystallize by the end of the conveyor belt, one would not necessarily be able to simply decrease the belt speed as that could bring the droplet rows into too close proximity for them to crystallize.

2.2.2. Operating Regimes

For mapping the operating space of our platform, we choose the industrially relevant API, artemether, which is used in the treatment of malaria.[32] We dissolve the API in ethyl acetate, which is partially miscible with our previously established yield-stress fluid system, an aqueous jammed suspension of poly(acrylic acid) microgels.[1,33] By varying nozzle diameter and injection flowrate, we can generate droplets of different nominal sizes at a fixed print speed. We are then able to observe different process outcomes as the belt speed is varied.

Figure 3a depicts the three categories of behavior we observe at the collection-end of the platform as the fluid film drains (i.e., once droplets have traveled a length L_B). When artemether solidifies, it becomes opaque, and so we use opacity as a proxy for whether solidification has occurred. We, thus, observe either apparent solidification of the droplets into opaque particles, translucent droplets that undergo little-to-no disruption as the surrounding film drains, and finally collapsed droplets that either burst at the fluid-air interface or adhere to the conveyor belt. Images of printed droplets as well as process outcomes for each combination of tested parameters are provided in the Supporting Information (Figures S2–S6, Supporting Information). Plotting each outcome, we visualize the operating regimes in Figure 3b. We rearrange Equations (3) and (4) to represent them on this space of belt speed versus droplet radius, and see that they nicely delineate the boundary between solid particles and liquid droplets when appropriate values of a and b are used. Note that the lower boundary was plotted using the approximation from Equation (2); the precise solution using Equation (1) deviates only slightly within the investigated range and does not affect the parameter b (see Figure S7, Supporting Information, for details).

Through our exploration of large droplet sizes, we also determine an empirical boundary of droplet size relative to film thickness. When unsolidified droplets are small relative to the film thickness (yellow outlined stars in Figure 3b), they are able to generally but not universally survive the process of film drainage and can continue to crystallize within the collection bath. When the initial diameter of the droplet surpasses approximately one-tenth of the overall fluid film thickness and the droplets are unable to undergo sufficient crystallization, widespread collapse is observed. The critical ratio of diameter to film thickness likely depends on numerous factors including the precise placement of the nozzle relative to the belt surface, the densities of the API solution and the crystallized material relative to the fluid film, and the dynamics of yield-stress fluid film drainage, but a deeper understanding of this ratio is outside the scope of the current work.

With these experiments, we have validated the proposed theoretical boundaries for the various operating regimes of our platform. Despite the necessity for adjustable parameters, knowing the shapes of these boundaries and how they may be tuned allows one to engineer similar platforms suited to many different material systems and any geometric constraints. Here, we achieve a maximum throughput of solid particles of 4.5 g h^{-1} (108 g per day) for a nominal initial droplet radius of 0.375 mm and a belt speed of 0.67 mm s^{-1} that results in a yield of 4.6 g L^{-1} of yield-stress fluid. However, this maximum throughput is

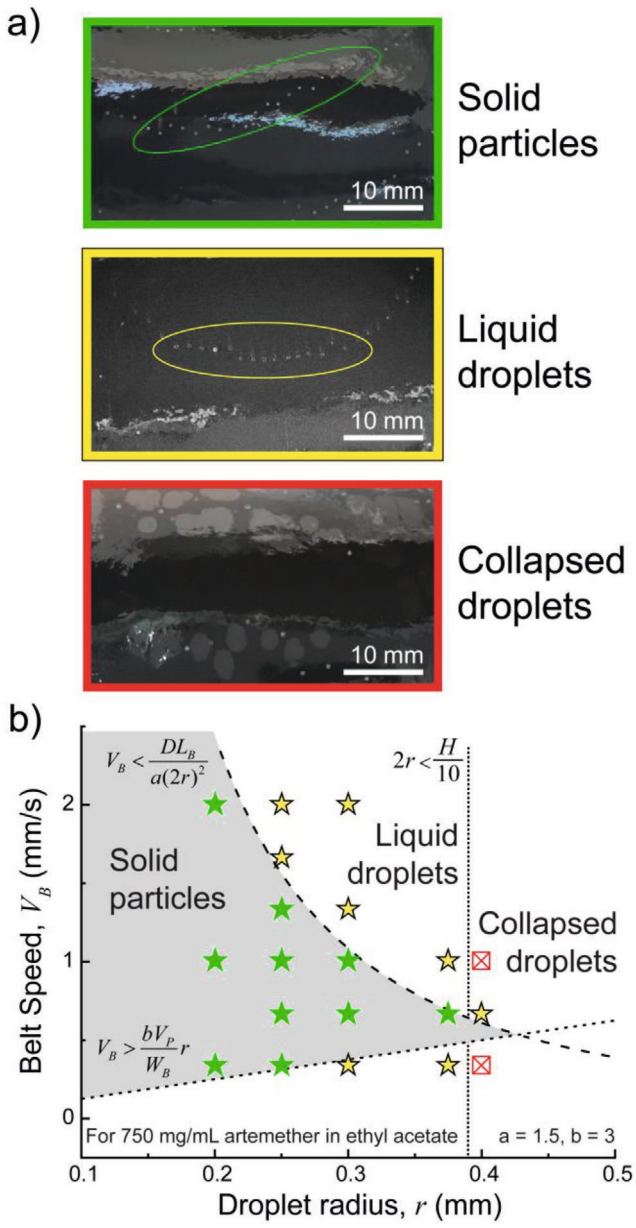

Figure 3. a) At the collection-end of the platform, we observe the printed material in three different states: apparent solidification into opaque particles (green, circled as a visual aid), translucent liquid droplets that undergo little-to-no disruption as the yield-stress fluid film drains (yellow, circled as a visual aid), and collapsed droplets bursting at the free surface or adhering to the belt (red). b) Processing map for continuous embedded droplet crystallization. The characteristic diffusion time and droplet spacing determine whether solid particles form (green stars) or droplets remain liquid (outlined yellow stars) at collection. Droplets with initial diameters of the same order of magnitude as the yield-stress fluid film that have not undergone sufficient solidification collapse as the film drains (red crossed boxes). Equations are plotted for the chosen material system and $V_P = 1000$ mm min^{-1}, $W_B = 40$ mm, $L_B = 600$ mm.

arrived at primarily due to our method for controlling droplet size. Rather than incrementally increasing nozzle size and flowrate, a more typical approach for maximizing throughput might be to target an initial droplet size first and design the geometric parameters around this. In this scenario, one would likely determine the nozzle sizes and injection flowrates that achieve the target droplet size for a maximum possible print speed, and would then need to make tradeoffs between geometric workplace constraints and throughput of yield-stress fluid. This process would be complicated by the current lack of a unified understanding of embedded droplet size as a function of flowrate, but we leave such a study to future work.

2.3. Characterization of Pharmaceutical Particles from Continuous Embedded Droplet Printing

With continuous embedded droplet printing, we gain the capability to produce gram-scale amounts of API particles as shown in **Figure 4**a. Video S2, Supporting Information, depicts how collected embedded particles can be easily recovered due to the ability to collapse the chosen yield-stress fluid via the addition of salt, allowing for further characterization. As seen in Figure 4b, the particles we obtain are indeed highly spherical (0.87 sphericity value, see Figure S8, Supporting Information) and uniform in size, suggesting high flowability. We are able to characterize the crystallinity of the obtained particles via powder X-ray diffraction (PXRD) and differential scanning calorimetry (DSC) as shown in Figure 4c,d, respectively; these indicate the presence of crystalline artemether of polymorph A.[34,35]

Finally, we characterize the flowability of the produced particles via powder rheology measurements. Using a shear cell setup, we obtain the incipient shear stresses for yielding to occur as a function of the applied normal stress for an initial consolidation stress of 3 kPa. Conventionally, a linear equation is fit to the data points below the consolidation normal stress and used to extract various flowability metrics including powder cohesion and the "flow function" (FF), which categorizes the overall flowability of the powder.[36,37] For our data, a single linear fit would result in a negative cohesion (vertical intercept) that is non-physical. As a result, we fit the yield-locus piecewise as shown in Figure 4e. Fitting greater and smaller Mohr's circles allows for the extraction of the maximum principal stress and unconfined yield strength, the ratio of which defines the FF.[36,37] Following the flowability classification defined by Schulze (FF < 1, not flowing; 1 < FF < 2 very cohesive; 2 < FF < 4, cohesive; 4 < FF < 10, easy flowing; FF > 10, free-flowing),[37] the powder we produced is well into the free-flowing range with a FF of 16.9, significantly surpassing the flowability of the pre-processed powder (see Figure S9, Supporting Information, for comparison).

3. Conclusions

Here, we presented a new platform for continuous embedded droplet printing. This platform expands the utility and functionality of embedded droplet printing, allowing its application in areas of continuous materials discovery, screening, and manufacturing. We apply this new platform towards the synthesis of pharmaceutical particles, where the absolutely quiescent environment of embedded droplets allows for the production

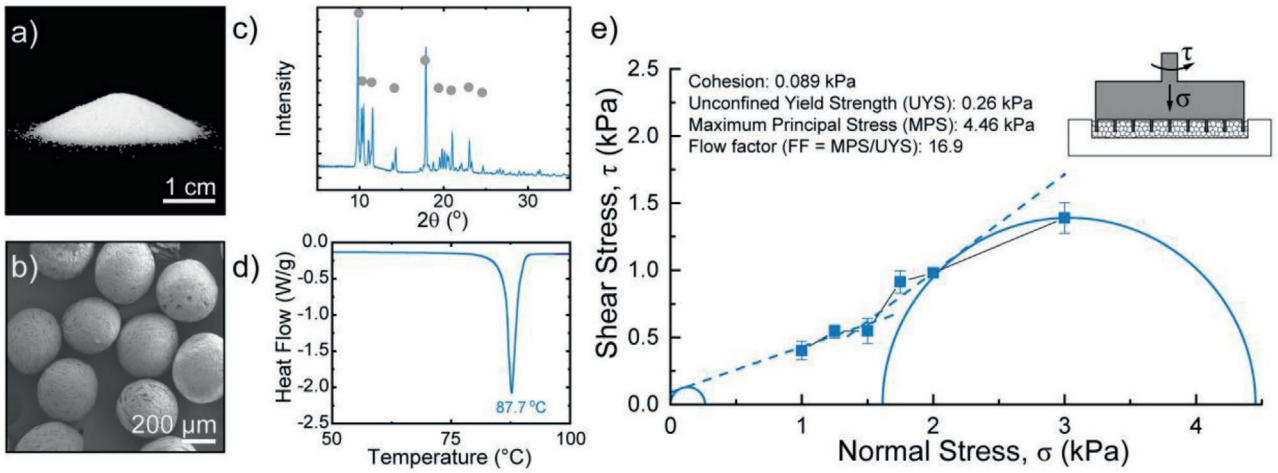

Figure 4. The continuous embedded droplet printing platform enables manufacturing of highly spherical, uniform pharmaceutical particles with superior flowability and processability. a) Macroscale image and b) field emission SEM image of particles of artemether, an industrially relevant API, synthesized via the presented platform. c) PXRD (gray circles indicate the characteristic peaks of polymorph A) and d) DSC thermogram of the particles depicted in (a) and (b), indicating the crystallinity of the artemether. e) Incipient shear stress of powder flow as a function of the applied normal stress. Inset schematic depicts the test setup with a 1 mL shear cell. Fits to the data allow for determination of the flow factor that classifies the powder as "free-flowing."

of crystallized particles that are as uniform and spherical as possible. We validated the proposed theoretical boundaries for antisolvent crystallization using an industrially relevant API, and maximized the mass throughput for a subset of printing parameters. We then demonstrated the superior morphology and flowability of the obtained crystalline particles, properties that are fundamental to the manufacturability and performance of drug products. Using the operating space and boundaries that we map out, we envision that similar systems may be engineered to enable precise, rapid, customized, and distributed manufacturing of drug particles with superior flowability.

4. Experimental Section

Materials: Carbopol 980 (cross-linked polyacrylic acid particles) was obtained from Lubrizol. Ultrapure water (18.2 MΩ) was obtained from a Sartorius H2OPRO-DI-T arium pro purifier. Sodium hydroxide (221465), Dow Corning high-vacuum silicone grease (Z273554), and sodium chloride (S5886) were purchased from Sigma-Aldrich. Artemether (A2190-25G) was purchased from Tee Hai Chem Pte Ltd. Ethyl acetate (HiPerSolv CHROMANOFORM for HPLC, ≥99.8%) was purchased from VWR International and used as received.

Material Preparation: Aqueous jammed suspensions of polymer microgels were prepared by mixing Carbopol 980 powder in ultrapure water at a concentration of 0.1 wt%. This solution was mixed for 30 min before being neutralized to pH 7 using a 1 M sodium hydroxide solution. This solution was placed in a vacuum chamber to remove air bubbles. The API-loaded injected phase was prepared by dissolving 750 mg of artemether per milliliter of ethyl acetate.

Continuous Platform: The Dobot magician robotic arm and conveyor belt were purchased from Servo Dynamics Pte Ltd. Large elastic bands were attached to the surface of the conveyor belt in layers using vacuum grease to form side walls with a nominal height of 8 mm and a center open-channel with a nominal width of 50 mm. Grease was also applied to the surface of the conveyor belt to facilitate drainage of the yield-stress fluid film. Flat-tipped stainless steel needles were purchased from either Nordson Advanced Technology Pte Ltd. or Taobao in nominal sizes of (inner diameter/outer diameter in millimeters) 0.108:0.235, 0.21:0.42, 0.44:08, 0.72:1.08, and 1.5:1.8. Nozzles were mounted to the end of the Dobot robotic arm and connected via poly(tetrafluoroethylene) tubes (inner diameter 1 mm) purchased from Cole Parmer to a 2.5 mL glass syringe (Hamilton GASTIGHT) purchased from Sigma-Aldrich mounted in a Harvard Apparatus syringe pump (PHD ULTRA 70-3007) purchased from ITS Science & Medical Pte Ltd. Aqueous yield-stress fluid was deposited on the belt from a reservoir via a BT100S peristaltic pump through a flexible 1 cm silicone tube. The tube end was clamped at belt height ≈5 cm from the front of the belt. A flexible piece of plastic was attached to the surface of the tube in contact with the belt to span the width of the open channel, helping fluid spreading and ensuring no backflow occurred. For printing, the nozzle end held by the Dobot arm was positioned a nominal height of 4 mm above the surface of the conveyor belt and such that the effective belt length was 60 cm. All droplets were printed at a speed of 1000 mm min^{-1} and a printing width of 40 mm (5 mm clearance on either side of the pattern). The fluid film was primed and delivered by having the peristaltic pump deposit yield-stress fluid at a volumetric flowrate calculated as channel width (50 mm) multiplied by wall height (8 mm) multiplied by belt speed for a given experiment. Droplets of nominal radius 0.2 mm were printed with a nozzle size (ID/OD) 0.108:0.235 mm at an injection flowrate of 10 µL min^{-1}. Droplets of nominal radius 0.25 mm were printed with a nozzle size (ID/OD) 0.21:0.42 mm at an injection flowrate of 50 µL min^{-1}. Droplets of nominal radius 0.3 mm were printed with a nozzle size (ID/OD) 0.44:0.8 mm at an injection flowrate of 50 µL min^{-1}. Droplets of nominal radius 0.375 mm were printed with a nozzle size (ID/OD) 0.72:1.08 mm at an injection flowrate of 100 µL min^{-1}. Droplets of nominal radius 0.4 mm were printed with a nozzle size (ID/OD) 1.5:1.8 mm at an injection flowrate of 200 µL min^{-1}. See Supporting Information for representative images of each droplet printing experiment and process outcome. Particles and used bath material were collected in a large beaker. To collapse the bath, a volume of 1 M NaCl solution approximately equal to 5% of the volume of the bath was added followed by agitation of the bath. Particles were collected via pipette and rinsed three times with ultrapure water and vacuum dried at room temperature for at least 12 h prior to characterization. All printing experiments were performed using a custom-made LabVIEW program detailed in Section S1, Supporting Information.

Characterization of Pharmaceutical Particles: The characterized pharmaceutical particles in Figure 4 were printed with a nozzle size (ID/OD) 0.44:0.8 mm, at a belt speed of 0.67 mm s^{-1}, and injection

flowrate of 50 μL min^{-1}, to have an initial droplet radius of 0.3 mm. Raw artemether powder was characterized as-received. All samples were prepared for scanning electron microscopy (SEM) on conventional stubs with a silicon wafer surface and were coated with ≈10 nm of platinum by sputter coating. A field-emission scanning electron microscope (JEOL JSM-6700F) at 5 kV accelerating voltage was used to image the particles. ImageJ was used to analyze the sphericity of the imaged particles. Polymorphic characterization of particles was analyzed using DSC and PXRD to examine their crystallinity. An X-ray diffractometer (Bruker; D8 Advance) was operated at 40 kV, 30 mA, and at a scanning rate of 1.06° min^{-1} over a range of 2θ from 2.5–30°, using a Cu radiation wavelength of 1.54 Å. For DSC, a TA Instruments DSC25 apparatus was used. Approximately 5 mg of sample was crimped in a sealed aluminum pan and heated at 5 °C min^{-1} in the range of 40–120 °C using an empty sealed pan as a reference. Powder rheometry experiments were performed on an FT4 rheometer from Freeman Technology using a 1 mL shear cell fixture and a pre-consolidation normal stress of 3 kPa. Experiments were repeated thrice to obtain standard deviation error bars. Fitting to shear stress data was performed using OriginPro 2019.

Supporting Information

Supporting Information is available from the Wiley Online Library or from the author.

Acknowledgements

The authors thank Dr. Denise Ng from the Singapore-MIT Alliance for Research and Technology for assistance with the characterization of pharmaceutical particles and for technical discussions regarding pharmaceutical crystallization. This research was supported by the National Research Foundation, Prime Minister's Office, Singapore under its Campus for Research Excellence and Technological Enterprise program. Financial support was also provided by the Pharmaceutical Innovation Programme Singapore (grant number A19B3a0012).

Conflict of Interest

The National University of Singapore has filed a provisional patent application on behalf of A.Z.N., S.A.K., and P.S.D. based on the research in this study.

Data Availability Statement

The data that support the findings of this study are available from the corresponding author upon reasonable request.

Keywords

crystallization, droplets, microfluidics, particle synthesis, pharmaceuticals, powder, yield-stress fluids

Received: December 14, 2020
Revised: February 1, 2021
Published online: March 6, 2021

[1] A. Z. Nelson, B. Kundukad, W. K. Wong, S. A. Khan, P. S. Doyle, *Proc. Natl. Acad. Sci. USA* **2020**, *117*, 5671.
[2] A. Z. Nelson, K. S. Schweizer, B. M. Rauzan, R. G. Nuzzo, J. Vermant, R. H. Ewoldt, *Curr. Opin. Solid State Mater. Sci.* **2019**, *23*, 100758.
[3] H. L. Hernandez, J. W. Souza, E. A. Appel, *Macromol. Biosci.* **2021**, *21*, 2000295.
[4] E. A. Appel, M. W. Tibbitt, M. J. Webber, B. A. Mattix, O. Veiseh, R. Langer, *Nat. Commun.* **2015**, *6*, 6295.
[5] J. E. Mealy, J. J. Chung, H. H. Jeong, D. Issadore, D. Lee, P. Atluri, J. A. Burdick, *Adv. Mater.* **2018**, *30*, 1705912.
[6] J. A. Lewis, *Adv. Funct. Mater.* **2006**, *16*, 2193.
[7] A. K. Grosskopf, R. L. Truby, H. Kim, A. Perazzo, J. A. Lewis, H. A. Stone, *ACS Appl. Mater. Interfaces* **2018**, *10*, 23353.
[8] B. M. Rauzan, A. Z. Nelson, S. E. Lehman, R. H. Ewoldt, R. G. Nuzzo, *Adv. Funct. Mater.* **2018**, *28*, 1707032.
[9] W. Wu, A. DeConinck, J. A. Lewis, *Adv. Mater.* **2011**, *23*, H178.
[10] A. N. Beris, J. A. Tsamopoulos, R. C. Armstrong, R. A. Brown, *J. Fluid Mech.* **1985**, *158*, 219.
[11] H. Emady, M. Caggioni, P. Spicer, *J. Rheol.* **2013**, *57*, 1761.
[12] M. Beaulne, E. Mitsoulis, *J. Non-Newtonian Fluid Mech.* **1997**, *72*, 55.
[13] Y. Zhang, Q. Zhao, D. Yuan, H. Liu, G. Yun, H. Lu, M. Li, J. Guo, W. Li, S.-Y. Tang, *Lab Chip* **2020**, *20*, 4592.
[14] L. Cai, J. Marthelot, P. T. Brun, *Proc. Natl. Acad. Sci. USA* **2019**, *116*, 22966.
[15] C. W. Visser, T. Kamperman, L. P. Karbaat, D. Lohse, M. Karperien, *Sci. Adv.* **2018**, *4*, eaao1175.
[16] S. Liao, Y. He, D. Wang, L. Dong, W. Du, Y. Wang, *Adv. Mater. Technol.* **2016**, *1*, 1600021.
[17] L. Cai, J. Marthelot, C. Falcón, P. M. Reis, P. T. Brun, *Soft Matter* **2020**, *16*, 3137.
[18] H. J. Mea, L. Delgadillo, J. Wan, *Proc. Natl. Acad. Sci. USA* **2020**, *117*, 14790.
[19] Q. Zhang, N. Willis-Fox, C. Conboy, R. Daly, *Mater. Horiz.* **2021**, *8*, 19.
[20] W. Spreen, S. L. Ford, S. Chen, D. Wilfret, D. Margolis, E. Gould, S. Piscitelli, *J. Acquired Immune Defic. Syndr.* **2014**, *67*, 481.
[21] Y. Kawashima, M. Imai, H. Takeuchi, H. Yamamoto, K. Kamiya, T. Hino, *Powder Technol.* **2003**, *130*, 283.
[22] Y. Kawashima, F. Cui, H. Takeuchi, T. Niwa, T. Hino, K. Kiuchi, *Powder Technol.* **1994**, *78*, 151.
[23] S. Chattoraj, C. C. Sun, *J. Pharm. Sci.* **2018**, *107*, 968.
[24] K. Pitt, R. Peña, J. D. Tew, K. Pal, R. Smith, Z. K. Nagy, J. D. Litster, *Powder Technol.* **2018**, *326*, 327.
[25] E. W. Q. Yeap, A. J. Acevedo, S. A. Khan, *Org. Process Res. Dev.* **2019**, *23*, 375.
[26] T. Gu, E. W. Q. Yeap, Z. Cao, D. Z. L. Ng, Y. Ren, R. Chen, S. A. Khan, T. A. Hatton, *Adv. Healthcare Mater.* **2018**, *7*, 1700797.
[27] R. Fortt, R. Tona, P. M. Martin-Soladana, G. Ward, D. Lai, J. Durrant, N. Douillet, *J. Cryst. Growth* **2020**, *552*, 125908.
[28] D. Zhang, S. Xu, S. Du, J. Wang, J. Gong, *Engineering* **2017**, *3*, 354.
[29] B. Wood, K. P. Girard, C. S. Polster, D. M. Croker, *Org. Process Res. Dev.* **2019**, *23*, 122.
[30] R. J. Davey, A. M. Hilton, J. Garside, *Chem. Eng. Res. Des.* **1997**, *75*, 245.
[31] E. Yeap Wan Qi, *Ph.D. Thesis*, National University of Singapore, Singapore **2018**.
[32] E. B. Esu, E. E. Effa, O. N. Opie, M. M. Meremikwu, *Cochrane Database Syst. Rev.* **2019**, *2019*, CD010678.
[33] J. M. Piau, *J. Non-Newtonian Fluid Mech.* **2007**, *144*, 1.
[34] Y. Zhang, Q. Liu, D. Zhang, Y. Jiang, *Huagong Xuebao* **2011**, *62*, 2958.
[35] J. Xu, V. Singh, X. Yin, P. Singh, L. Wu, X. Xu, T. Guo, L. Sun, S. Gui, J. Zhang, *Drug Dev. Ind. Pharm.* **2017**, *43*, 372.
[36] L. X. Liu, I. Marziano, A. C. Bentham, J. D. Litster, E. T. White, T. Howes, *Int. J. Pharm.* **2008**, *362*, 109.
[37] D. Schulze, *Powders and Bulk Solids: Behavior, Characterization, Storage and Flow*, Springer, Berlin **2008**.